Centrifuge study on the use of protective walls to reduce tunnelling-induced damage of buildings

Geyang Song[a,*], Alec M. Marshall[b]

[a] *Department of Engineering Science, University of Oxford, Parks Road, Oxford, OX1 3PJ, United Kingdom. Formally Faculty of Engineering, University of Nottingham, University Park, NG7 2RD Nottingham, United Kingdom.*

[b] *Faculty of Engineering, University of Nottingham, University Park, NG7 2RD Nottingham, United Kingdom.*

Abstract

Tunnel excavation in urban areas causes ground movements that could damage existing nearby piled structures. In practice, to protect structures from tunnelling-induced damage, a stiff protective wall can be constructed between the tunnel and the adjacent piled structure. In this paper, results from four hybrid geotechnical centrifuge tests (where data are coupled between the centrifuge and numerical models) are used to quantify the effect of protective walls on reducing the impact of tunnelling on an adjacent framed building with four piles. Two protective walls with different embedded depths are considered: a 'shallow' wall with its toe at the tunnel axis depth and a 'deep' wall with its toe below the tunnel invert. Compared to the 'no-wall' case, the 'deep' protective wall is shown to significantly reduce uneven pile settlements, structural distortions, and load transfer (through the building) between piles; the 'shallow' wall is shown to have little benefit. Data from the

*Corresponding author

Email addresses: geyang.song@eng.ox.ac.uk (Geyang Song), alec.marshall@nottingham.ac.uk (Alec M. Marshall)

instrumented walls and piles are used to explain the dominant mechanisms at play and investigate how the load is redistributed within the piles.
Keywords: Tunnelling, Centrifuge modelling, pile, structure, protective wall

Highlights

- Effect of protective walls on reducing the impact of tunnelling on piled structures.
- Protective walls can reduce the tunnelling induced ground movements on the retained side.
- Protective wall could reduce pile settlement and structural distortions.
- The impact of the protective walls on pile shaft resistance development.

1. Introduction

Tunnel construction frequently takes place close to existing piled structures. The associated stress relief can affect the equilibrium state and cause uneven settlements among the piles, potentially leading to the superstructure's damage. Geotechnical centrifuge testing has been widely used to study the tunnel-pile-structure interaction (TPSI) problem (Hong et al., 2015; Jacobsz, 2003; Lee et al., 1999). Generally, piles have been either individually loaded or rigidly connected, neglecting the effect of structure stiffness on pile loading. Recent centrifuge tests conducted by Franza et al. (2019) and Song and Marshall (2020b) have accounted for the effect of structural stiffness and demonstrated that the structure stiffness affects the load transfer among piles during tunnel volume loss, with a resulting change in the shaft resistance and load distribution within individual piles.

In practice, a 'protective wall' can be built between the building and the tunnel to reduce or prevent structure damage (Ledesma and Alonso, 2017). As described by Di Mariano et al. (2007), this stiff wall generally consists of a row of bored piles. The case studies reported by Di Mariano et al. (2007) and Ledesma and Alonso (2017) focus mainly on the structure deformation and ground displacements; no data are available to assess the load transfer between piles or the changes in shaft resistance along the piles that occur with tunnelling. In addition, there are very few experimental studies which have considered this problem. Bilotta (2008) conducted centrifuge tests to investigate the effect of a diaphragm wall on soil movements caused by tunnel volume loss in over-consolidated clay; the study did not explicitly include a structure or foundation system. To the authors' knowledge, no experimental studies have been conducted which include all the interacting components, i.e. tunnel, protective structure, pile foundations, and structure.

This paper presents results from four geotechnical centrifuge tests to study the tunnel-wall-pile-structure interaction (TWPSI) problem. Two model protective walls were tested in the centrifuge with different embedded depths; a 'shallow' wall where the toe of the wall was located at the tunnel springline and a 'deep' wall where the toe was located below the tunnel invert. Fibre Bragg grating strain sensors were used to measure axial forces and bending moments along the depth of the piles and protective walls, respectively. The effect of protective walls on tunnelling-induced ground movements is analyzed first, using greenfield and 'no-wall' test cases as a reference. The deformation of the protective walls and the bending moments induced along the walls with tunnel volume loss are then studied. The effect of protective walls on pile settlements is analyzed using the method from Xu et al. (2020), the deformation and damage of the building are assessed. Finally, the impact of the protective walls on how shaft resistance develops along the piles during tunnel volume loss is presented.

2. Centrifuge experimental setup

Four centrifuge tests, summarised in Table 1, were conducted on the University of Nottingham Centre for Geomechanics' (NCG) 2 m radius, 50 g-tonne geotechnical centrifuge at an acceleration of 80 times gravity (i.e., 80 g). Figure 1 shows the test geometry in model scale for tests TWPSI 1 and 2, including the simulated (numerically; discussed later) steel frame structure configuration (in prototype scale). Test TPSI is identical to the test layout shown in Figure 1 except that the protective wall is not included; hence results can be directly compared against tests TWPSI 1 and 2. Note that results from test TPSI were also presented in Song and Marshall (2020b) (labeled as TPSI3 in that paper). Test GF is a greenfield tunnelling test, where piles and the protective walls were not included, used as a reference for comparison with all other tests.

The general test geometry was identical in all tests, with the four piles added to the GF test geometry to obtain the TPSI test, then the protective wall added to obtain the TWPSI tests. For the TWPSI tests, two protective wall lengths were considered: the first with a depth of 207 mm, equivalent to the depth of the tunnel axis (termed the 'shallow' wall; test TWPSI 1), and the second with a depth of 297 mm, with its base one tunnel radius beneath the tunnel invert (termed the 'deep' wall; test TWPSI 2). The protective walls were located between the tunnel and first pile of the pile group, with the central axis of the wall being 55 mm away from the tunnel axis ($d_w = 55$ mm).

2.1. Centrifuge model

The centrifuge model layout for test TWPSI 2 is illustrated in Figure 2. The centrifuge strongbox has internal dimensions of 150 mm width, 700 mm length, and 500 mm height. An eccentric rigid boundary mechanical (eRBM) model tunnel (Song et al., 2018; Song and Marshall, 2020a) was used to replicate tunnelling ground loss, with an initial diameter of 90 mm and a clear distance of 130 mm between the bottom of the tunnel and the strongbox base. The model tunnel can provide non-uniform radial displacements around the tunnel lining, causing maximum soil displacement at the tunnel crown and

Table 1: Summary of centrifuge tests (model scale)

Test label	Final tunnel volume loss $V_{l,tf}$	Structure stiffness †	Length of the wall L_w
GF	2.8 %	NA	NA
TPSI	2.8 %	F	NA
TWPSI 1	3.1 %	F	207 mm
TWPSI 2	3.0 %	F	297 mm

GF = greenfield; TPSI = tunnel-pile-structure interaction

TWPSI = tunnel-wall-pile-structure interaction

† NA = not applicable; F=Structure with full stiffness

no displacements at the tunnel invert.

For tests TPSI and TWPSI 1 and 2, a hybrid modeling approach was adopted to simulate the effect of the connected frame structure, known as the coupled centrifuge-numerical modeling (CCNM) technique (Idinyang et al., 2018; Franza and Marshall, 2018a). In these tests, the structural analysis is conducted in a numerical simulation (a virtual structural domain), which, for a given input of pile head displacements, solves for pile head load based on the characteristics of the building. The soil, piles, and protective walls were all included in the centrifuge model (the physical geotechnical domain). Further details of the adopted CCNM technique for these tests are provided in Song and Marshall (2020b). The structural numerical model was developed using ABAQUS (Hibbitt, 2002), where a five-storey steel frame building was

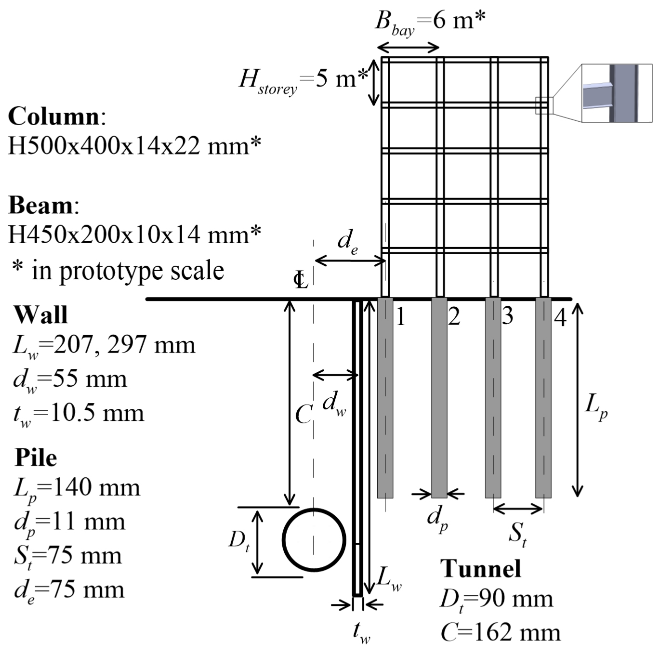

Figure 1: Tests TWPSI1 and 2 layout in model scale

considered. A linear elastic constitutive model was used for the building columns and beams (see Figure 2 for dimensions), with a Young's modulus $E = 210\,\mathrm{GPa}$ and a Poisson's ratio of $\nu = 0.3$. Note that beams are connected to the web of the columns instead of the flange, which could provide greater bending stiffness; see Figure 1 for the column orientation. The building elements such as stairways, façades, and bracings were not considered in the numerical model. Based on variable ($7.5\,\mathrm{kN/m^2}$) and permanent ($3\,\mathrm{kN/m^2}$) loads given by Eurocode (Gulvanessian et al., 2009) (specifications for storage purpose buildings), an initial load of 2,364 kN was applied to the two inner piles (piles 2 and 3; see Figure 1) and 1,630 kN for the two outer piles (piles 1 and 4; loads in prototype scale). In the numerical model, a hinged joint was assumed at the base of the columns (where they would connect to the pile caps) since the real rotational stiffness at this connection is not known (consistent with Idinyang et al. (2018)). Franza et al. (2017) illustrated that the influence of this pile-structure connection is minor for framed buildings with isolated pile heads, as is the case in this study, hence the impact of this assumption is minimal.

The pile head loads were applied to the model piles via the loading system illustrated in Figure 2. The loading system was controlled under a LabVIEW environment, which enables either force or displacement control of the pile heads. Each model pile was connected to a linear actuator (driven by a stepper motor) via a loading shaft. A die spring was used between the driving actuator and a loading shaft to reduce the sensitivity of the load response to movements of the actuator. A 5-kN in-line load cell was connected to the pile to measure the pile head load. To measure the pile settlement, four linear variable differential transformers (LVDTs) were placed at the base of the supporting frame with their armatures resting on plates fixed to the pile heads.

Two cameras (Dalsa nano-m4020, Teledyne DALSA, Canada) were placed in front of the acrylic wall, and GeoPIV-RG (Stanier et al., 2015) was used to calculate soil displacements from the obtained images. The precision of the GeoPIV-RG measurements was evaluated using the procedure applied by Marshall and Mair (2011); Song and Marshall (2020a); two images were taken successively at elevated gravity (80 g) during a time when no soil displacements were imposed (i.e. no tunnel volume loss) and horizontal and vertical displacements were assessed based on 53 260 subset patches from the images. The standard deviation of horizontal and vertical displacements was found to be 1.57 μm and 1.77 μm, respectively.

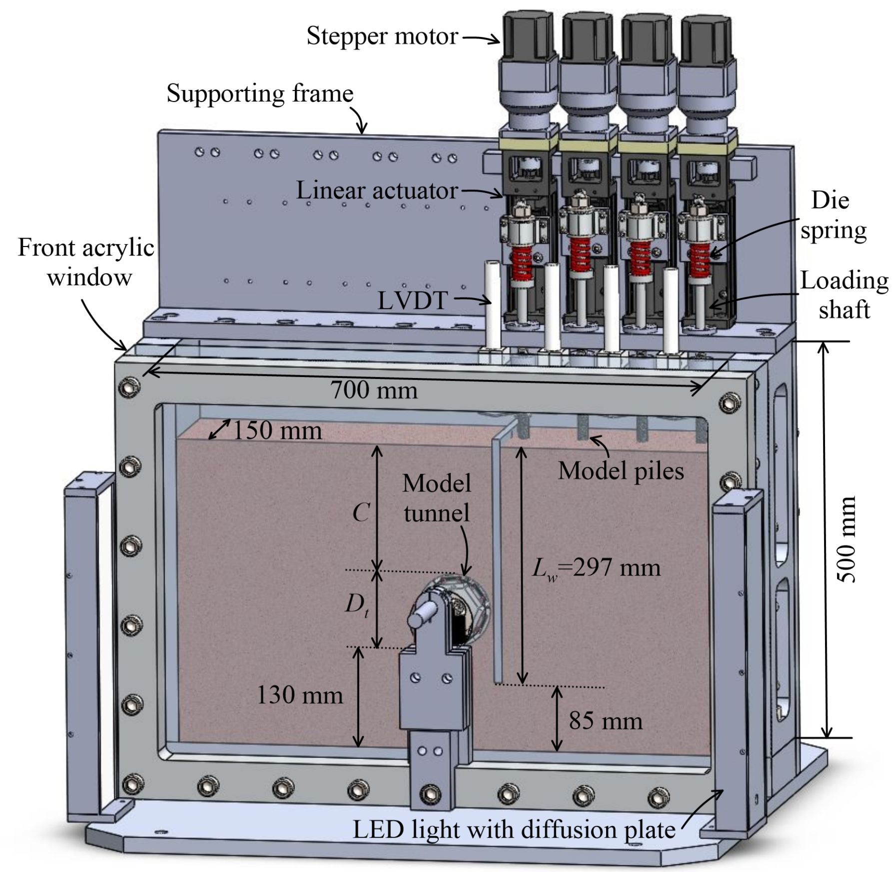

Figure 2: Centrifuge model layout for test TWPSI 2

2.2. *Model piles and protective walls*

The model piles used in this study were made from hollow aluminum tubes with an outer diameter of 10 mm and a wall thickness of 1 mm. To increase the interface roughness, sand (the same as the main soil body) was bonded to the surface and toe of the model piles using epoxy, which gave a final pile diameter of 11 mm ($\approx$ 0.8 m in prototype scale). In practice, a

0.8 m diameter concrete pile has an axial stiffness $EA = (10 - 14) \times 10^3$ MN, assuming the concrete has a Young's modulus $E = 20 - 28$ GPa. The hollow aluminum model piles (ignoring the effect of epoxy/sand coating) have an axial rigidity $EA = 19.4 \times 10^3$ MN in prototype scale, which is slightly higher than the 0.8 m full-scale concrete pile.

A 10 mm thick aluminum plate was used in the centrifuge test to model the protective wall. The width of the aluminum plate is 148 mm, where the width of the strongbox is 150 mm. At prototype scale, the aluminium model protective wall has a flexural rigidity $EI = 34.8 \times 10^3$ MNm^2. In practice, an unreinforced 0.8 m thick concrete wall has a flexural rigidity of $EI = 10 - 14 \times 10^3$ MNm^2 (assuming the same Young's modulus range as used previously). Therefore, in terms of bending rigidity, the aluminum plate represents a 1-1.2 m thick unreinforced concrete wall. The sand was bonded to the model wall's surface and base to increase the interface roughness, consistent with the method used for the model piles.

2.3. Fibre Bragg Grating sensors and calibration

In this study, Fibre Bragg Grating (FBG) sensors were used to measure the axial force along the model piles, as well as the bending moments along the model protective walls. Unlike conventional strain gauges, where the gauges are normally bonded to the outer surface of the model pile or wall, which can create an irregular outer surface profile and change the model surface roughness, FBG sensors can be installed inside the model pile or wall due to their relatively small size and lightweight nature. The FBG (an intrinsic sensing element) can be photo-inscribed into a silica fiber using an excimer laser. The laser etches a certain length of the fiber at regular spacings

Λ (referred to as the 'grating pitch'). As described by Kersey et al. (1997), the basic principle of the FBG sensor is to measure the shift in wavelength of the light reflected by this grating (referred to as a 'Bragg') due to strain or temperature changes.

Figure 3 presents a schematic diagram of the FBG system adopted in this study (additional details are described in Song et al. (2021)). Two four-channel FBG interrogators (SmartScan SBI, Smart Fibres Ltd, Bracknell) with a wavelength range between 1528 to 1568 nm at a frequency of 2.5 kHz were used to measure the FBG wavelength shifts. Fiber optic splitters (couplers) were used to reduce the number of signals from the eight fibers (four piles each containing 2 fibers) down to four fibers for FBG interrogator (1). The splitters have an even split ratio from one input fiber to two output fibers. The FBG interrogators were mounted in the centrifuge data acquisition systems (DAS) cabinet, which, during centrifuge tests where the model on the centrifuge cradle experienced a nominal 80 g, the cabinet was exposed to g-levels of 4-7 g. Data generated from the FBG interrogators was transferred via an Ethernet cable to an onboard gigabit switch (1). The gigabit switch (1) was connected to a fiber optic rotary joint via a subscriber connector (SC) optical cable, and the output data was then transferred to gigabit switch (2), which was located in the centrifuge control room and linked to a computer. This setup allows the real-time logging of the FBG data from the control room during centrifuge tests.

For each model pile, two FBG optical fibers were attached along opposing inner surfaces of the aluminum tubes. The elongation strain of the FBG sensors can be directly correlated to the physical strain along a model pile.

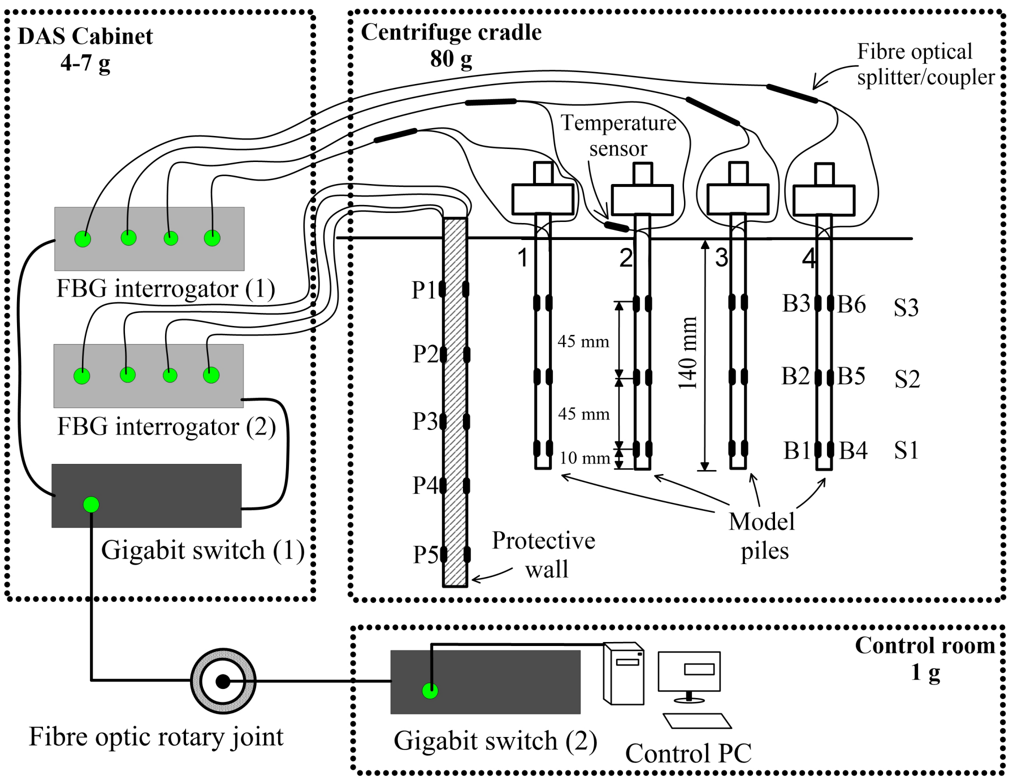

Figure 3: FBG sensor system adopted in this study

The FBG sensors were made from a single-mode optical fiber, with each fiber containing three FBG sensors (denoted B1-B3 or B4-B6, see Figure 3) written by an excimer laser with a center wavelength of 1530, 1535, 1540 nm or 1545, 1550, 1560 nm. For pile 2, one additional FBG sensor was used to measure the ambient air temperature during centrifuge tests (temperature change will cause additional straining of the model pile due to thermal expansion or contraction). Song et al. (2021) showed that for the same setup described here, an ambient air temperature increase of about $0.7\,°C$ caused an increase of $\approx 0.3\,°C$ within a buried pile, which resulted in a variation of axial force within the pile of $\approx 12\,\mathrm{N}$. This estimated force due to temperature change was corrected from readings presented later in this paper. Note that this correction mainly affects the absolute value of measured forces; there was little effect on the measurement of change in pile axial forces during the tunnel volume loss process because the change in temperature was negligible during this time (most temperature change occurring during the centrifuge spin-up process).

The axial force of each pile was directly correlated with the FBG wavelength shift ($\Delta\lambda_B$) through calibration tests. A Global Digital Systems (GDS) load frame was used to apply an axially compressive force to each pile within a temperature-controlled room, with each calibration exercise repeated a minimum of three times. The calibration provides a linear relationship between the FBG wavelength shift ($\Delta\lambda_B$) and the applied load. At a given depth (S1, for example; see Figure 3), the average reading from the two opposing FBG sensors (B1 and B4 for location S1) were used to calculate the axial force of the pile at that location.

For model protective walls, FBG sensors were installed within channels machined into opposing sides of the wall at the middle and quarter width of the wall (in the out-of-plane direction, i.e., along the tunnel length). Brass U-channels were installed to protect the FBG sensors from soil pressures during centrifuge tests, which could affect FBG readings (additional sensor installation details are provided in Song et al. (2021)). To reduce the interface friction between the protective wall ends and the strongbox's front/back walls in the centrifuge tests, Polytetrafluoroethylene (PTFE) stripes were placed on the front and back faces of the protective walls. Similar to the axial force calibration for the piles, the bending moment of the model protective wall at a particular FBG sensor location (P1-P5, see Figure 3 for numbering) was directly correlated with an FBG wavelength shift ($\Delta\lambda_B$). A three-point bending moment test arrangement was used to conduct the calibration tests within a temperature-controlled room.

A linear relationship between the change in wavelength (i.e., the differences of changes in wavelength from FBG sensors on opposing sides of the tube at a given location) and the applied bending moment was obtained. Temperature correction is not needed for the wall because bending moments are calculated as the differences in FBG wavelength shift on both sides of the wall, and the temperature effects will be identical for these two FBG sensors; hence the temperature effect is self-compensated. Further details of the bending moment calibration procedures and results are described in Song et al. (2021).

2.4. Soil and model preparation

A fine-grained silica sand known as Leighton Buzzard Fraction E sand was used for the tests. The sand has a typical average diameter D_{50} = 0.14 mm and maximum (e_{max}) and minimum (e_{min}) void ratios of 1.01 and 0.61, respectively. In addition, the sand has a specific gravity $G_s = 2.64$ and a coefficient of uniformity $C_u = 1.58$.

To prepare the model, the strongbox was placed with its back wall facing downwards and the model tunnel secured within the back wall, thus allowing the sand to be poured in the direction of the tunnel longitudinal axis, consistent with the work of earlier researchers (Vorster, 2006; Marshall, 2009; Zhou, 2015; Franza, 2016; Farrell, 2010). Prior to sand pouring, for tests TWPSI 1 and 2, the protective model wall was placed in the designated position, then two temporary supports were secured inside the strongbox at locations corresponding to the intended soil surface. For tests GF and TPSI, a single temporary support was used. The sand was then prepared according to a methodology calibrated to achieve a relative density of $I_d \approx 90\%$. After sand pouring, the front acrylic window was bolted to the strongbox, the box was rotated to its upright position, and the temporary supports were removed.

For tests TWSI and TWPSI 1 and 2, to replicate non-displacement piles, the model piles were pushed into the sand at 1 g, starting with pile 1, closest to the tunnel, and moving outwards to pile 4. Given the low-stress conditions within the soil during this process, the disturbance of the soil during pile installation is considered to be minimal. Additionally, since the method is consistent between tests, results can be readily compared. A support frame was used to ensure the piles were pushed vertically, which was temporarily connected to the strongbox and removed after pile installation. The pile loading system was then fixed to the top of the strongbox, and the model piles were connected to the linear actuators. Finally, the tunnel volume loss control system was installed, consisting of a gearbox, stepper motor, and LVDT (the detailed assembly is described in Song and Marshall (2020a)).

2.5. Testing procedure

For test GF, the centrifuge package was spun to 80 g in stages of 10 g, including three stabilisation cycles (going from 80 g to 10 g and then back to 80 g) which are conducted with the aim of achieving a consistent ground stress condition and improve the repeatability of results between tests. After the stabilisation cycles, the tunnel volume loss process was started, and images were taken at each interval of tunnel volume loss (0.18% $V_{l,t}$).

For tests TPSI and TWPSI 1 and 2, a 5 N vertical load was maintained at the pile head during centrifuge spin-up. This was done with the aim of achieving minimal relative displacement between the piles and the soil during centrifuge spin-up. The piles were then loaded to their designated working loads in 50 N stages, starting from pile 1 closest to the tunnel and moving sequentially outwards to pile 4. As previously mentioned, the outer piles 1 and 4 were loaded to 255 N and inner piles 2 and 3 were loaded to 370 N (see Figure 1 for pile numbering). The CCNM program communication protocols (Idinyang et al., 2018) were then activated, enabling the sharing of pile load and settlement data between the physical/geotechnical domain in the centrifuge and the virtual/structural domain in ABAQUAS, and giving control of the pile loading in the centrifuge to the outputs of the simulated structural system. An increment of tunnel volume loss causes ground movements, which are translated into pile settlements (which vary from pile to pile). The pile settlement data are communicated with the structural numerical model (ABAQUS) and the modified pile head loads are calculated based on the load redistribution within the simulated structure. These modified pile head loads are then fed back into the centrifuge model and the pile head loads are adjusted via the linear actuators (load controlled). These processes continue to cycle until a steady-state is reached. To ensure a minimal cycling time, a small increment of tunnel volume loss is used. Once a steady-state is reached, another increment of tunnel volume loss is initiated, and the process continues. Images were taken after every tunnel volume loss increment (after reaching a steady-state condition).

3. Results

3.1. The effect of protective walls on tunnelling-induced ground movements

Figure 4 shows the vertical and horizontal soil displacement contours for all tests (GF, TPSI, TWPSI 1 and 2) at a tunnel volume loss of $V_{l,t} = 2\%$. Note that, except for the greenfield GF test, the soil displacement data do not relate to a plane strain condition because the piles were located in the middle of the strongbox (75mm away from the acrylic window), and the displacement data were obtained from the soil at the acrylic window. The vertical and horizontal displacements in test TPSI (not plane-strain) are similar in shape and magnitude to test GF (plane-strain), which suggests that the displacements at the acrylic window in test TPSI were not affected by the piles. Considering this, and assuming that the piles have minimal effect on the response of the protective walls (there was also good agreement between bending moment data at the quarter and half width locations of the wall, indicating that the deformed shape of the wall was consistent across its width, which supports this assumption), the soil displacements in test TWPSI 1 and 2 can be compared directly with those of test GF.

For tests GF and TPSI, a concentrated vertical displacement zone above the tunnel crown is observed, along with zones of major horizontal displacements near the tunnel springline, which propagate toward the soil surface at an inclined angle. Similar observations of greenfield ground movements due to tunnelling were provided by Franza and Marshall (2019); Marshall (2012) using a water-filled, flexible lining (pressure-controlled) model tunnel; an assessment of the different ground movements obtained with pressure and displacement control model tunnels was provided in Song and Marshall (2020a)

For the 'shallow' wall test TWPSI 1, soil settlements 'behind' the wall (i.e., to the right; $x/D_t > 0.7$) are only slightly reduced compared to tests GF and TPSI, whereas for the 'deep' wall test TWPSI 2, soil settlements in this region are significantly less.

These observations can be directly related to the depth of the toe of the protective wall. The toe of the 'shallow' wall is located at the tunnel springline, where horizontal displacement in tests GF and TPSI are shown to be significant; hence the wall (at its toe) has little capacity to resist the ground movements initiated by tunnel ground loss and instead acts to average greenfield settlements that occur along with the depth of the wall (as noted by Franza and Marshall (2018b) for piles) and imposes a complicated pattern of horizontal displacements due to wall rotation, with little mobilisation of the wall's bending resistance. For the 'deep' wall in test TWPSI 2, the toe of the wall is located below the tunnel invert where greenfield displacements are very small (Zhou, 2015), hence the toe of the wall is relatively fixed, and the wall is able to resist soil displacements above the tunnel springline by mobilising its resistance to bending. Figure 4 shows a localised zone of horizontal displacements on the retained side of the wall at a depth of $z/z_t = 0.4-1.2$, indicating the bending of the wall near the tunnel springline, where greenfield horizontal displacements are greatest. Wall deformations and associated bending moments will be discussed in the next subsection.

In both tests TWPSI 1 and 2, the soil located 'in front' of the wall (i.e., to the left; $x/D_t < 0.7$) shows a 'tilted' chimney-like soil settlement mechanism, initiating from the wall-side of the tunnel crown and propagating towards the surface at the tunnel centreline. The magnitude of soil settlements above the tunnel is similar all tests, however the 'tilt' of the chimney-like settlement profile is somewhat more pronounced in test TWPSI 2. The wall also didn't have a significant impact on the magnitude of horizontal displacements above the tunnel, but did affect their distribution, with the 'zero' line propagating up from the tunnel crown in the direction of the shallow protective wall, whereas for the deep wall, the 'zero' line is shifted more uniformly towards the wall.

3.2. Protective wall response to tunnelling

The horizontal displacements (S_h) and bending moments of the walls (measured from the FBG sensors located along the middle width of the walls, corresponding to the location of the row of piles) with tunnel volume loss are shown in Figure 5. The FBG sensor data at the quarter with of the

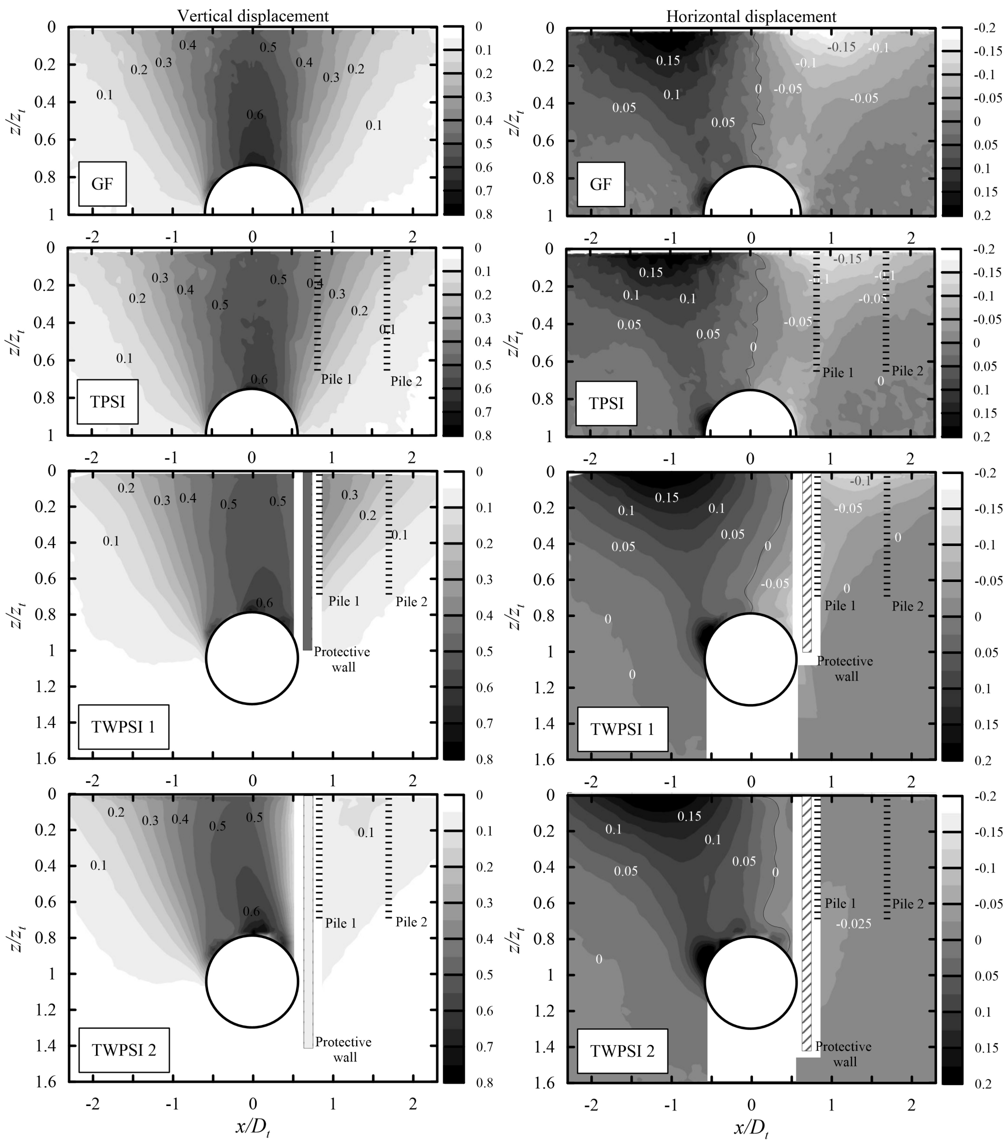

Figure 4: Contours of vertical and horizontal displacement (mm) at $V_{l,t} = 2\%$ (positive values are downwards and to the right)

wall showed very similar results to the data at the middle width of the wall (hence only the middle data is presented), which indicates good consistency of the bending response along the width of the wall. Therefore, the horizontal displacements S_h measured at the acrylic wall of the model box, presented in Figure 5, were taken as representative of the deformed wall shape along its entire width. In both tests TWPSI 1 and 2, some sand particles intruded into the gap between the toe of the model wall and the acrylic strongbox wall, rendering the obtained displacement data unreliable. As a result, based on the measured bending moments, the displacement data close to the toe of the walls were estimated (adapting the estimated displacement data to fit the measured bending moments).

For the 'shallow' wall (test TWPSI 1) where the toe of the wall was located at the tunnel springline ($z/z_t = 1$), with tunnel volume loss, the toe moved towards the tunnel, with horizontal wall displacements reducing towards the surface. The bending moment data indicates that the maximum bending moment is located at a depth of between $z/z_t = 0.6$ (at $V_{l,t} = 1\%$) and 0.8 (at $V_{l,t} = 3\%$; i.e. the depth of the maximum bending moment increases with tunnel volume loss).

For the 'deep' wall (test TWPSI 2) where the toe was located below the tunnel invert ($z/z_t = 1.43$) where tunnelling induced ground movements are negligible, with tunnel volume loss, the middle portion of the wall ($z/z_t = 0.8 - 1.0$) showed the greatest horizontal displacement towards the tunnel, whereas the upper portion of the wall moved away from the tunnel due to the bending action of the wall. The bending moment profile indicates that the moments in the upper portion of the wall are very small ($z/z_t = 0 - 0.4$), with

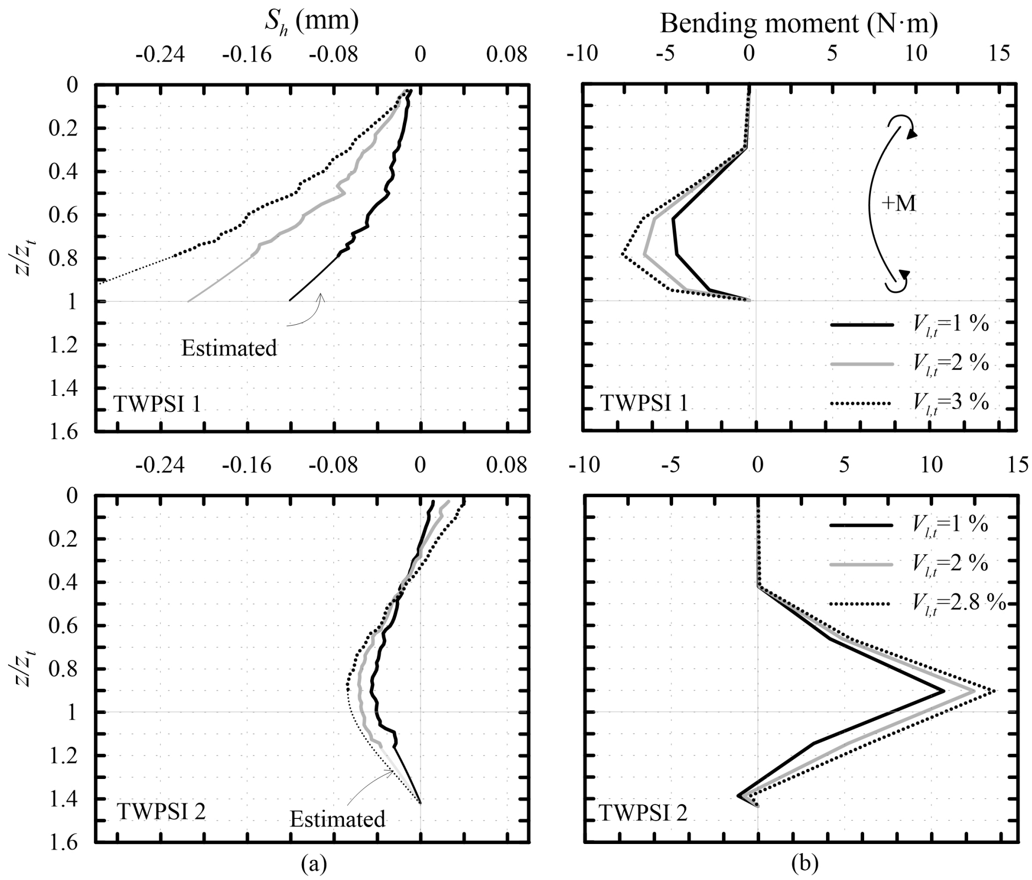

Figure 5: (a) Horizontal displacements and (b) bending moments along the wall with tunnel volume loss

the maximum positive bending moment located in the middle portion of the wall ($z/z_t = 0.8 - 1.0$). As discussed previously, the flexural rigidity of the model wall in prototype scale is greater than that of a 0.8 m thick unreinforced concrete wall; hence these results under-predict the deformations of a 0.8 m thick concrete wall.

To summarise, the deformed shape of the protective wall highly depends on the length of the wall with respect to the depth of the tunnel. For test TWPSI 1 ('shallow' wall), the tunnelling induced ground movements that caused the toe of the wall to move towards the tunnel, with little horizontal displacement occurring near the ground surface. For test TWPSI 2 ('deep' wall), the toe of the wall experienced limited displacement, and soil movement towards the tunnel occurred at a depth of $z/z_t = 0.8 - 1.0$, resulting in the wall bending towards the tunnel at this depth and away from the tunnel near the surface.

3.3. The effect of protective walls on pile settlement

Figure 6 shows the normalised pile head settlement (S_p/d_p) with tunnel volume loss for tests TPSI and TWPSI 1 and 2; note that the scale of the settlement for each pile is different, with the magnitude of settlements reducing with the distance from the tunnel (from pile 1 to 4). For test TWPSI 2 ('deep' wall), because the wall effectively reduced the soil movements behind the wall (see Figure 4), the settlement of the piles closes to the tunnel (piles 1 and 2) was significantly reduced when compared with the other two tests (TPSI and TWPSI 1). Test TPSI, with no protective wall, generally shows the greatest pile displacements (except for pile 4 where pile settlements in all three tests were similar). The 'shallow' wall in test TWPSI 1 is shown to have only a marginal reducing effect on pile settlements compared to test TPSI.

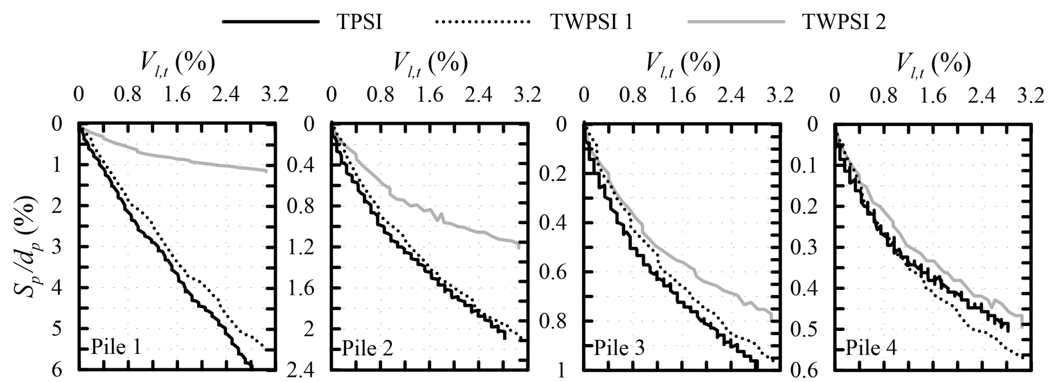

Figure 6: Pile head settlement with tunnel volume loss

The efficiency of the protective walls to reduce pile settlement at a given tunnel volume loss can be quantified using

$$\eta_{pw} = \frac{S_s - S_{pw}}{S_s} \times 100\,\% \tag{1}$$

where S is pile settlement, the superscripts pw stand for the use of the protective wall, and s refer to cases with the structure only (without the protective wall). An efficiency $\eta_{pw} = 0$ indicates that the protective wall had no effect on pile settlement (i.e., pile settlements match those from test TPSI).

Figure 7 presents the efficiency parameter η_{pw} of the piles with tunnel volume loss for tests TWPSI 1 and 2. For test TWPSI 1 ('shallow' wall), at lower values of tunnel volume loss ($v_{l,t} = 0.5-1.5\%$), the efficiency parameter for all four piles decreased as tunnel volume loss increased, indicating the effectiveness of the wall reduced. With further increase in tunnel volume loss ($V_{l,t} > 1.5\%$), the efficiency parameter increased slightly. Piles 1, 2 and 3 show similar values of efficiency (on average $\approx 10\%$), whereas pile 4 shows smaller values. Note, however, that the settlements of pile 4 are very small, which explains the obtained negative values of efficiency (the negative values for pile 4 were assumed as 0; see the grey line in Figure 7).

For test TWPSI 2 ('deep' wall), the magnitude of all four piles' efficiency parameter is considerably larger than test TWPSI 1, especially those piles located closer to the tunnel/protective wall. Pile 1 shows a steady increase in the efficiency parameter with tunnel volume loss. In contrast, for piles 2, 3 and 4, the trend is similar to that from test TWPSI 1, where the efficiency decreases from about $V_{l,t} = 0.5 - 1.5\%$ then increases or stays steady for higher volume losses ($V_{l,t} > 1.5\%$).

In general, the variation of the efficiency parameter is not very sensitive to tunnel volume loss. The length of the protective wall, as well as the distance between the pile and tunnel (x/D_t), have the dominant role. As a result, the average efficiency parameter $\overline{\eta_{pw}}$ (based on $V_{l,t} = 0.5- \approx 2.8\%$) for all four piles is plotted against the relative tunnel-pile position (x/D_t) in Figure 8 (a).For both tests, the average pile efficiency decreases with x/D_t.

Figure 8 (b) shows the normalised pile head settlement at a tunnel volume loss of $V_{l,t} = 2.8\%$, demonstrating the significant benefit of the 'deep' protective wall to reduce pile head settlement and, importantly from the perspective of structural distortion, the relative settlements between piles, compared to tests TWPSI 1 ('shallow' wall) and TPSI.

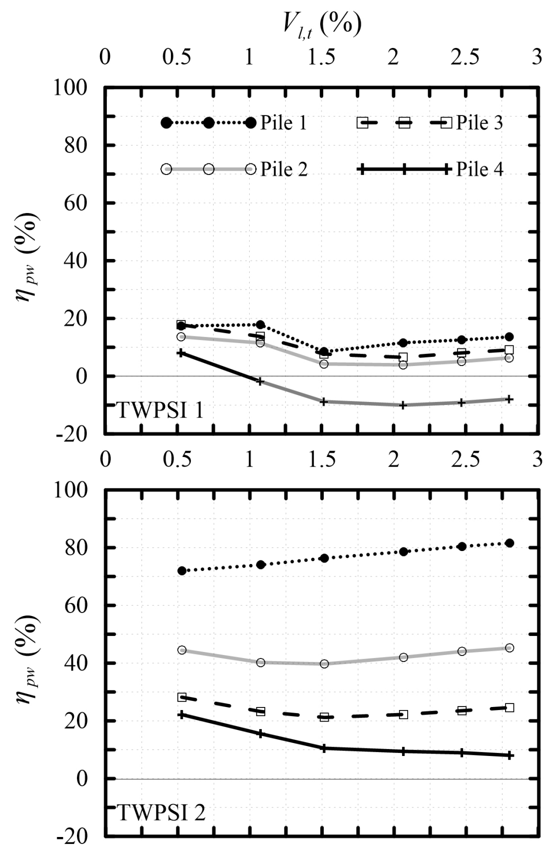

Figure 7: Efficiency parameter η_{pw} with tunnel volume loss

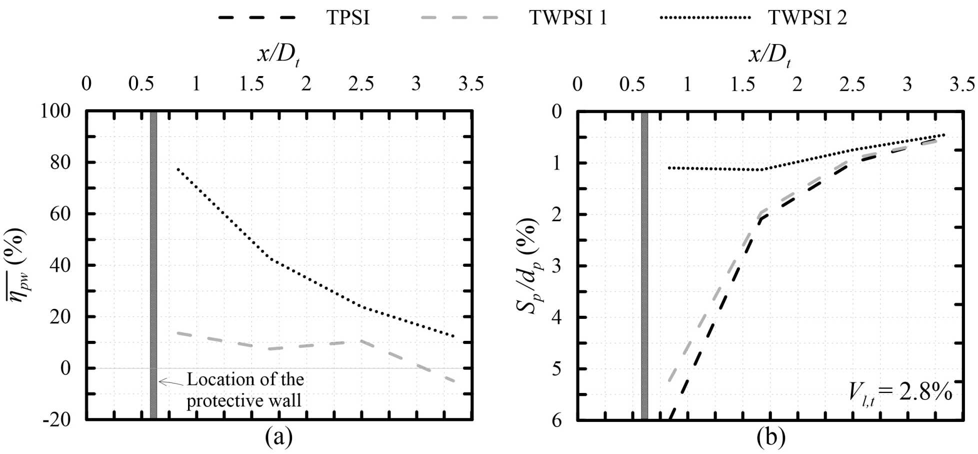

Figure 8: (a) average efficiency parameter $\overline{\eta_{pw}}$ and (b) normalised pile head settlement with respect to pile location

3.4. The effect of protective walls on building deformation and damage

Maximum tensile strain (ϵ_{max}) is commonly used to correlate with structure damage categories. Table 2 summarises the critical tensile strain and the categories of damage developed by Boscardin and Cording (1989).

The work done by Boone (1996); Elkayam and Klar (2019) distinguished the assessment of building deformation between bay and panel. To assess the maximum tensile strain (ϵ_{max}) within a structure (panel), Xu et al. (2020) suggested that the angular distortion parameter β [developed by Son and Cording (2005)] can be used, where $\epsilon_{max} \approx \beta/2$ when the horizontal elements within a building have a relatively high axial stiffness. The angular distortion parameter was initially used to calculate deformations within a building bay, however Xu et al. (2020) adopted the method to calculate β for individual panels based on the displacements at the top and bottom corners of each

Table 2: Critical tensile strain and categories of damage after Boscardin and Cording (1989)

Category of damage	Level of damage	Limiting tensile strain (%)
0	Negligible	0-0.05
1	Very slight	0.05-0.075
1-2	Slight	0.075-0.15
3-4	Moderate to severe	0.15-0.3
4-5	Severe to very severe	>0.3

panel (points A, B, C and D in Figure 9).

$$\begin{aligned} \text{Angular distortion } (\beta) &= \text{Slope (S)} - \text{Tilt } (\theta) \\ \text{Slope (S)} &= \frac{S_{v,A} - S_{v,B}}{B_{bay}} \\ \text{Tilt } (\theta) &= \frac{(S_{h,A} - S_{h,D}) + (S_{h,B} - S_{h,C})}{2H_{storey}} \end{aligned} \tag{2}$$

where B_{bay} is the length of a bay, H_{storey} is the height the storey, S_v and S_h are the vertical and horizontal displacements of a structural joint, respectively (at points A, B, C, and D in Figure 9).

Figure 10 shows, for tests TPSI and TWPSI 1 and 2, the angular distortion β of the panels in each bay at a tunnel volume loss of $V_{l,t} = 2.8\%$. For panels in bay 1 (closest to the tunnel), tests TPSI and TWPSI 1 show positive values of β, deforming as illustrated in Figure 9, with β being greater for test TPSI than TWPSI 1. Moving upwards through the building stories, the

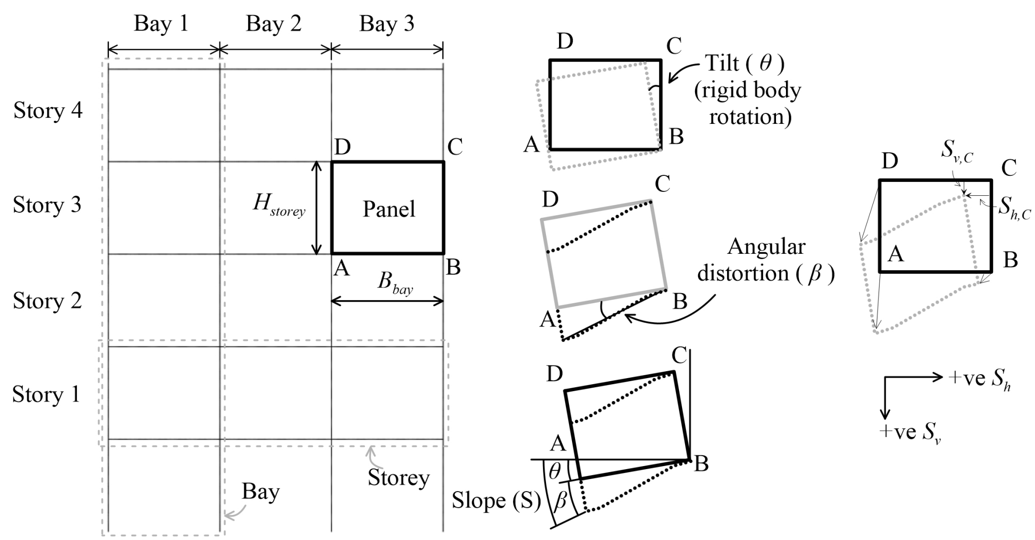

Figure 9: Illustration of the structural layout and calculation of angular distortion after Son and Cording (2005)

values of β are shown to decrease somewhat. For test TWPSI 2, the panels in bay 1 experienced limited distortion and β does not vary with storey. Note that a negative value of β indicates that the distortion acts to reduce the slope S of the panel that is rotated by θ anti-clockwise (i.e. slope S would be less than rotation θ). For panels in bays 2 and 3, β in tests TPSI and TWPSI 1 are negative, whereas β values are all positive for test TWPSI 2, indicating a change in the direction of the distortion compared to the panels in bay 1. For tests TPSI and TWPSI 1, panels in bays 2 and 3 experience less distortion than in bay 1, with a marginal decrease in absolute values of β with storey number, similar to the panels in bay 1. It is interesting that the 'deep' protective wall in test TWPSI 2 not only significantly reduced building distortions compared to the 'short' and no-wall tests, but that it also 'flipped' the trend in direction of distortion β within the bays of the building.

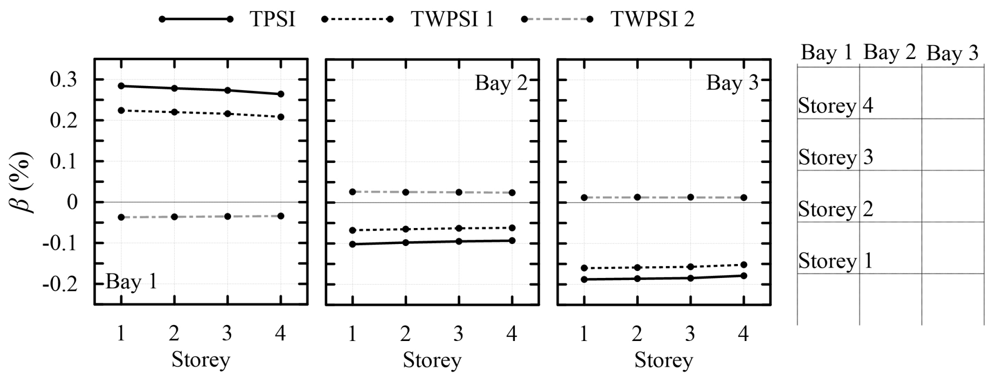

Figure 10: Angular distortion of building panels at a tunnel volume loss of $V_{l,t} = 2.8\%$

The above data indicate that the most significant angular distortions occurred in the lower-most storey 1. To discuss the effect of tunnel volume loss on angular distortion, Figure 11 shows the development of β with tunnel volume loss for panels within storey 1. All three tests show a near-linear increase in the absolute value of angular distortion with tunnel volume loss. Test TPSI shows the greatest rate of increase in β with tunnelling, followed by tests TWPSI 1 and 2. For tests TPSI and TWPSI 1, at a given tunnel volume loss, panels in bay 1 underwent the greatest value of angular distortion, followed by bay 3 and bay 2.

To further demonstrate the effect of protective walls on structural damage, Figure 12 shows the structure deformed shape at a tunnel volume loss of $V_{l,t} = 2.8\%$ for all three tests. Markers are used within panels to indicate the category of damage based on Table 2, along with a number indicated the value of β. At $V_{l,t} = 2.8\%$, for tests TPSI and TWPSI 1, the highest category of damage is 2 (slight damage) for all stories in the exterior bays (and 1 in

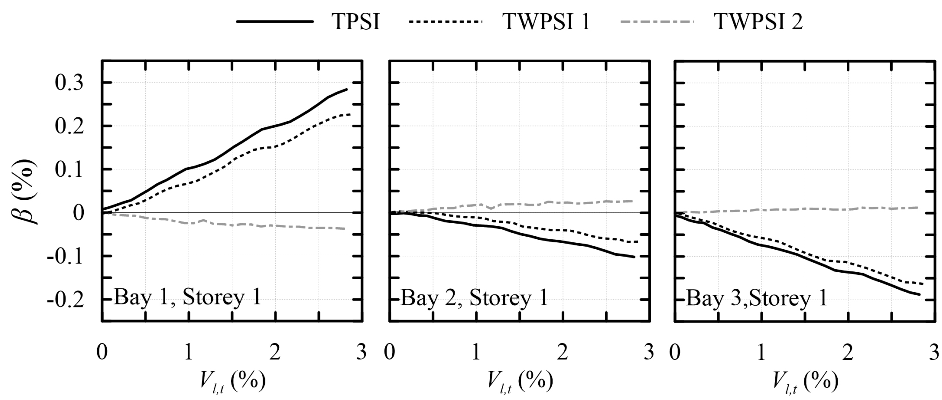

Figure 11: Angular distortion of building panels in storey 1 with tunnelling

the interior bay), whereas for test TWPSI 2, the category of damage for the entire building is 0 (negligible).

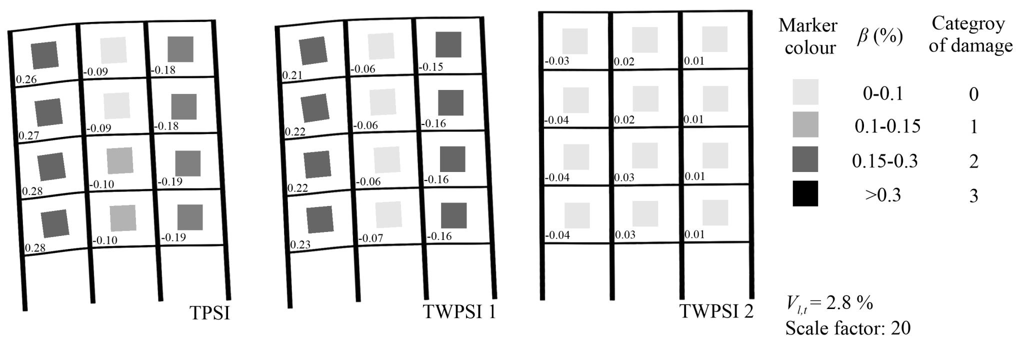

Figure 12: Structure deformed shape and level of damage at $V_{l,t} = 2.8\%$

A relatively high value of tunnel volume loss ($V_{l,t} = 2.8\%$) was adopted for illustrative purposes in Figure 12 to demonstrate the beneficial effect of the 'deep' protective wall based on category of damage. In practice, a design value of tunnel volume loss is more typically about $V_{l,t} = 1\%$; at this tunnel volume loss, for the scenarios considered here, a category of the building damage of 0 (negligible) was obtained in all three tests.

3.5. The effect of protective walls on pile head load transfer

Prior to tunnel volume loss, piles were loaded to the designated load (255 N for outer piles 1 and 4; 370 N for inner piles 2 and 3; refer to pile numbering in Figure 1). With tunnel volume loss, the axial force along the pile is affected by two dominant mechanisms (Song and Marshall, 2020b): (1) the effect of tunnelling induced ground movements and stress relief (referred to as Mechanism T for tunnelling), and (2) change in pile head load due to the stiffness effect of the connected structure (referred to as Mechanism S for structure; achieved in these tests using the CCNM application). Note that pile-pile interaction is not considered in this study.

Figure 13 shows pile head load versus tunnel volume loss for tests TPSI and TWPSI 1 and 2. For test TPSI, pile 1 experienced the most significant decrease in pile head load with tunnel volume loss. The reduced pile 1 head load was transferred, through the connected structure (Mechanism S), to the adjacent piles 2 and 3, whereas pile 4, due to a global building rotation, shows a decrease in head load. For test TWPSI 1 ('shallow' wall), the pile load transfer mechanism is similar to test TPSI. For test TWPSI 2 ('deep' wall), the magnitude of load transfer among piles is minimal due to the small levels of pile and structure displacements, illustrated previously. In addition, the load transfer direction is opposite to tests TPSI and TWPSI 1 (i.e. pile 1 head load increased in TWPSI 2, but decreased in test TPSI and TWPSI 1). This is because the building distortion (β) direction in test TWPSI 2 was opposite to the other two tests. The load transfer, predominately in tests TPSI and TWPSI 1, causes changes in pile shaft resistance, discussed in the next subsection.

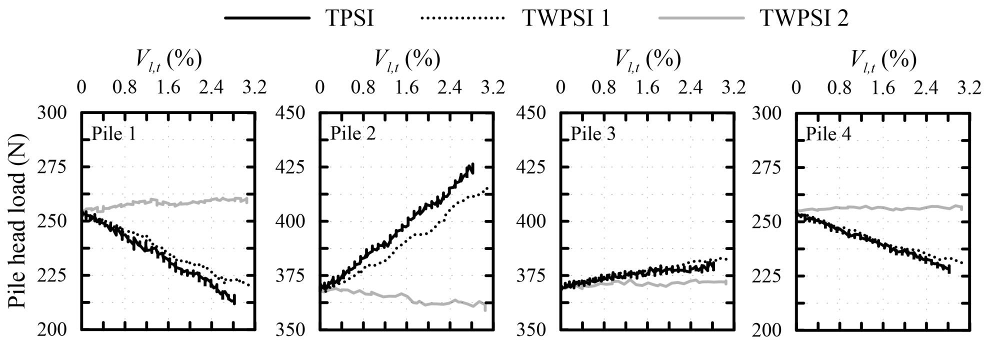

Figure 13: Pile head load with tunnelling

3.6. *The effect of protective walls on pile axial force and shaft resistance*

Figure 14 presents the axial force along the piles with tunnel volume loss for tests TPSI and TWPSI 1 and 2. Note that the axial pile load at the soil surface is greater than the pile head load (measured with the load cell) due to the effect of the self-weight of the pile, a connector and the LVDT armature plate located below the load cell; the weights of these components, along with the g-level at their locations (≈ 73 g), were used to obtain the pile axial load at the ground surface. After pile loading ($V_{l,t} = 0\%$), axial forces in the upper portion of some piles are slightly higher than the pile head load. This is because, during centrifuge spin-up, the soil settlements around the upper and middle portions of some piles were greater than pile settlements, acting to pull the piles downwards. During pile loading to the designated working load, the pile settlement in the upper portion was insufficient to cause a reversal of shear stress direction (refer to Song and Marshall (2020b) for a more in-depth discussion).

The response of pile 1 in tests TPSI (no protective wall) and TWPSI 1 (‘shallow’ wall) was similar, with a decrease in the load at the pile head (due

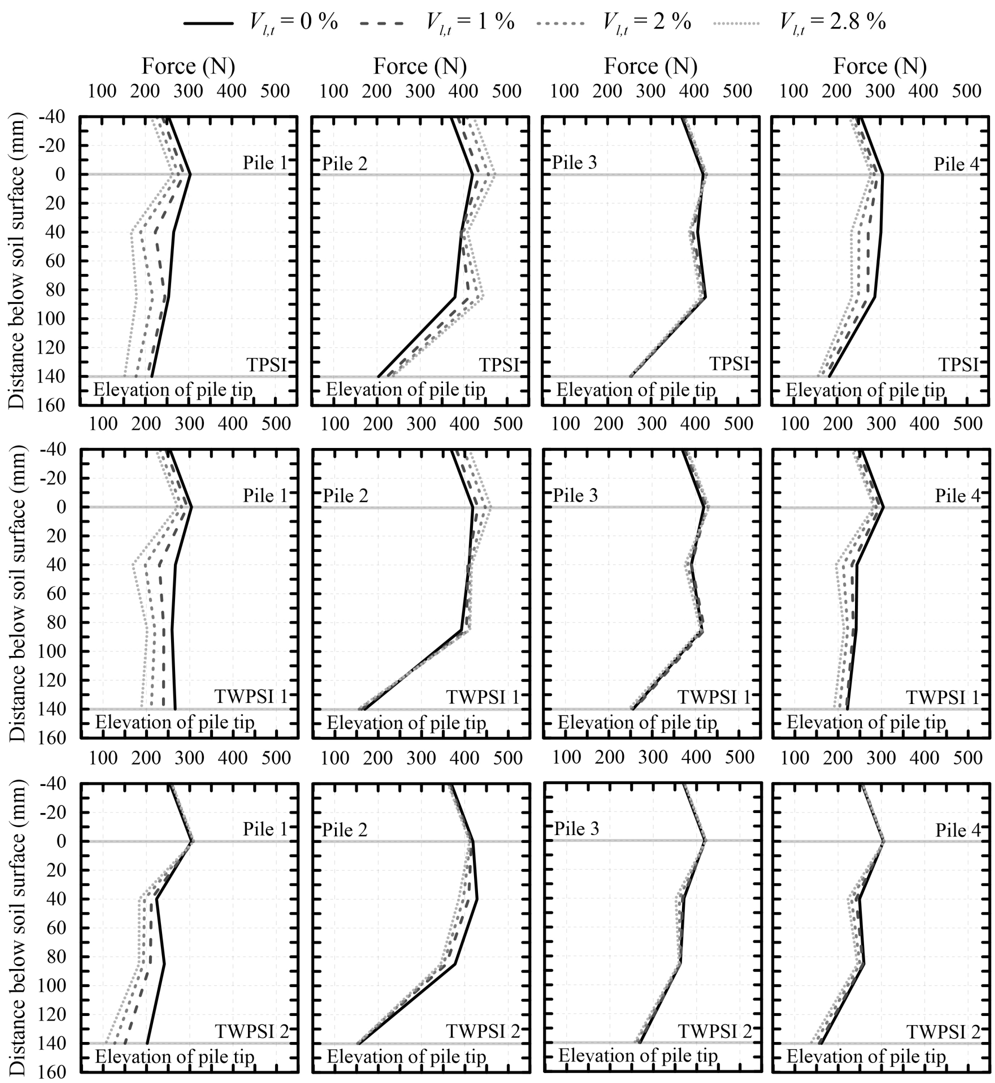

Figure 14: Axial force along piles with tunnel volume loss

to Mechanism S) and a reduction in the load at the pile toe with tunnel volume loss (due to Mechanism T). In contrast, the pile head load of pile 1 in test TWPSI 2 ('deep' wall) increased by a small amount, whereas the pile end bearing load decreased with tunnelling, indicating an increase in shaft resistance. It is interesting that, though the 'deep' protective wall was able to effectively reduce the settlements of pile 1, the end-bearing load was still significantly affected. This can be related to the deformed shape and bending profile of the 'deep' wall (Figure 5), where the pile tip (at $z/z_t = 0.68$) is within the zone where the wall bends towards the tunnel.

For pile 2 in test TPSI, the pile head load increased with tunnelling (Mechanism S), as well as the axial force along the pile and at its toe, indicating that the end bearing force mainly took the increased pile head load. For pile 2 in test TWPSI 1 ('shallow' wall), the pile head load also increased with tunnelling, but unlike pile 2 in test TPSI, the loads along the pile increased slightly and, at its toe, show little change. These results indicate that the shaft resistance mainly took the increased pile head load in test TWPSI 1. For pile 2 in test TWPSI 2 ('deep' wall), the loads at the pile head and toe experienced minimal change with tunnel volume loss. The axial force in the middle and upper portions of the pile reduced, indicating some degree of load transfer along the pile; this will be discussed in more detail later in this subsection.

The change in axial force along pile 3 in all tests was minimal. For pile 4 in tests TPSI and TWPSI 1, pile head load decreased with tunnelling; the structure stiffness (Mechanism S) enabled a global anti-clockwise rotation of the building (see Figure 12). Consequently, the axial force along the pile was reduced. For pile 4 in test TWPSI 2, the pile head load remained relatively constant with tunnelling, with axial forces along the pile reducing by a small amount.

In a general case of pile loading (no tunnelling), an increase in pile head load will increase the shaft resistance along the pile shaft and base (the proportion of shaft/base load increase depending on the pile and soil types); Figure 15 illustrates an idealised situation of change in pile shaft/base resistance as well as the relative displacement between the soil (S_v) and pile (S_p) during pile loading. With the increase in pile head load, the pile settles more than the soil, mobilising upwards (positive) shaft resistance as well as base resistance. The idealised scenario in Figure 15 does not consider tunnelling induced ground movements or the more complex pre-loaded condition of the piles in the centrifuge tests; it will be used as a reference for discussion and understanding of results obtained from the centrifuge tests.

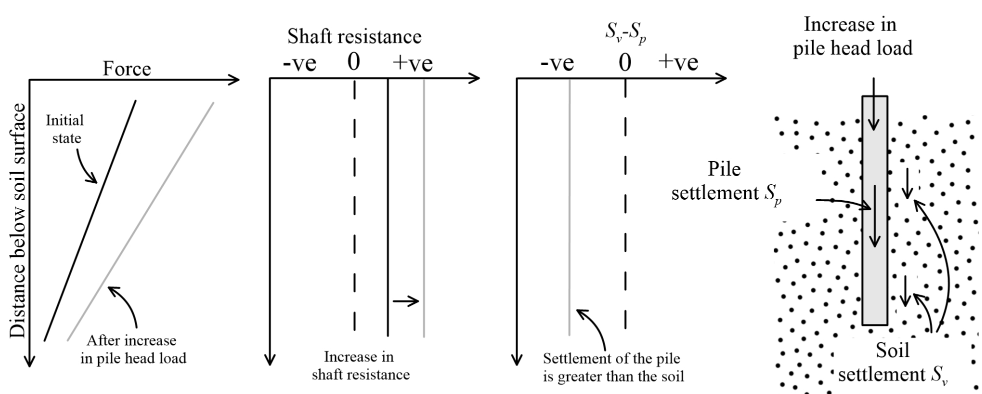

Figure 15: Illustration of shaft resistance development with the increase in pile head load under an idealised case

Figure 16 shows the shaft resistance along the piles at four stages of tunnel volume loss for all tests. As noted previously, prior to tunnel volume loss, but after the piles were loaded to the designated working loads ($V_{l,t} = 0\%$), negative shaft resistance developed in some piles due to the centrifuge spin-up process (the soil tends to pull the piles downwards near the surface during centrifuge spin-up).

To help understand the data of shaft resistance along the piles with tunnelling from Figure 16, Figure 17 plots, at a tunnel volume loss of $V_{l,t} = 2.8\%$, relative soil-pile settlements. The soil settlements were obtained from image analysis of the soil at the acrylic wall at locations (x/D_t) corresponding to the piles. As discussed in Section 3.1, the soil movements at the acrylic wall were not significantly affected by the piles' existence (the greenfield GF test displacements matched well to those from test TPSI). The relative soil-pile settlements in Figure 16 therefore relate to the approximated difference between pile settlements and the soil settlement that would otherwise occur in the absence of the piles (but accounting for the effect of both the tunnel and the protective wall, which are continuous across the width of the centrifuge model). The relative settlement is defined as $S_v - S_p$, where S_v is soil settlement along the length of the pile and S_p is the pile settlement (assumed constant). Due to the camera field of view, only S_v of piles 1, 2, and 3 could be measured.

For pile 1 in test TPSI, Figure 17 shows negative relative settlement along the depth of the pile, indicating that the pile settled more than the soil. Therefore, the shaft resistance in the middle and lower portions of the pile is expected to increase with tunnel volume loss (similar to the shear mechanism described in the idealised case in Figure 15). Referring to Figure 16

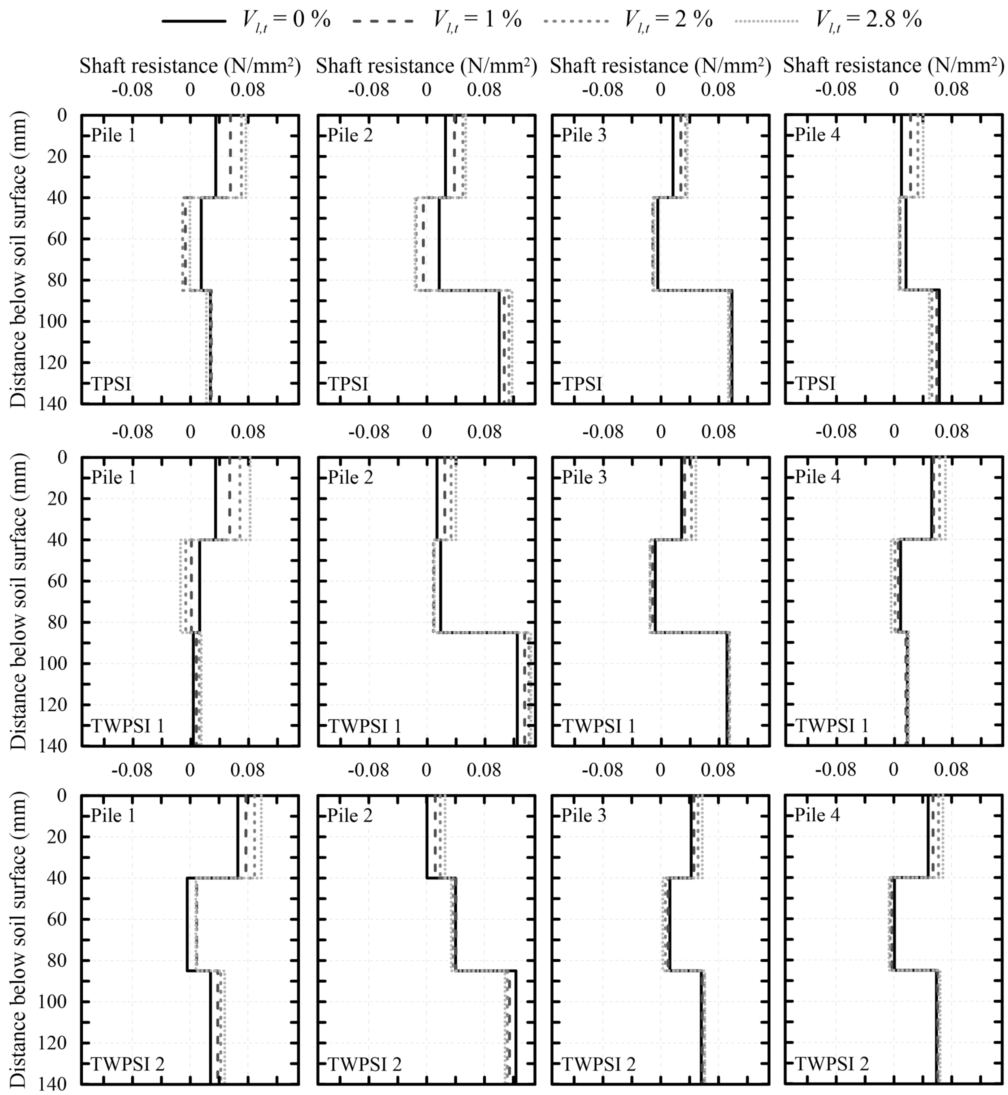

Figure 16: Shaft resistance along piles with tunnel volume loss

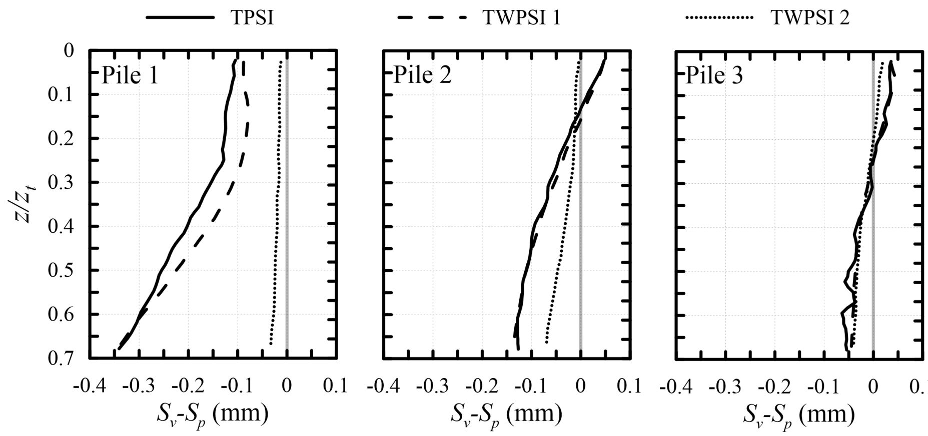

Figure 17: Relative pile-soil settlements at a tunnel volume loss of $V_{l,t} = 2.8\%$

at a tunnel volume loss of $V_{l,t} = 2.8\%$, the shaft resistance only increased in the upper portion of the pile; it decreased in the middle and lower portions of pile 1 (contradicting the idealised case). This can be explained by the reduction in radial stress around pile 1 that occurs as a result of tunnel volume loss (Mechanism T), which primarily affects the lower and middle portions of pile 1 (as demonstrated in Song and Marshall (2020a) for the greenfield condition using finite element analyses). Although the lower portion of pile 1 experienced greater relative soil pile displacement, the mobilised shaft resistance at the lower portion of the pile decreased due to reduced radial stress around the lower portion of the pile.

For pile 1 in test TWPSI 1 ('shallow' wall), similar to the pile in test TPSI, the pile's relative settlement in Figure 17 is greater than the surrounding soil. Therefore, the shaft resistance (Figure 16) in the upper portion of the pile increased (similar to pile 1 in test TPSI). Unlike pile 1 in test TPSI, a small increase in shaft resistance in the lower portion of the pile is observed, presumably because the 'shallow' wall provided some level of protection against the effect of the tunnel in reducing ground stresses around the pile.

Referring to Figure 17, pile 1 in test TWPSI 2 settled more than the surrounding soil, but the magnitude is less than pile 1 in tests TPSI and TWPSI 1, especially near the pile toe. Despite the small relative pile-soil displacement for pile 1 in test TWPSI 2, the shaft resistance in the lower portion of the pile (Figure 16) shows a greater increase than for pile 1 in test TWPSI 1. Therefore, it can be surmised that the 'deep' protective wall was more effective at preventing the ground stress relief (Mechanism T) in the lower portion of pile 1 than the 'shallow' protective wall.

For pile 2 in test TPSI, the pile head load (see Figure 13) and the pile end bearing load (see Figure 14) increased with tunnel volume loss. Pile 2 in test TWPSI 1 responded similarly, except that the increase in pile end bearing load is minimal with tunnel volume loss, indicating that the increased pile head load was mainly taken by the shaft resistance. Figure 16 indicates that the shaft resistance in the upper and lower portions of pile 2 increased with tunnelling for tests TPSI and TWPSI 1 (similar to the idealised pile load case presented in Figure 15), whereas the shaft resistance in the middle portion decreased (contradicting the idealised case). Referring to Figure 17, pile 2 in tests TPSI and TWPSI 1 settled more in the middle and lower portions of the pile than the soil. Therefore, under a given radial stress level (idealised case), the shaft resistance in the middle and lower portions of pile 2 in these tests is expected to increase. The decrease in shaft resistance in the middle portion of pile 2 in tests TPSI and TWPSI 1 therefore suggests that the radial stress in the middle portion of pile 2 was affected by the tunnelling induced ground movement (decrease in radial stress; Mechanism T), whereas the lower portion was not affected.

In test TWPSI 2, the pile 2 head load (Figure 13) and the pile end bearing load (Figure 14) showed little change, yet there was a decrease in shaft resistance in the lower portion of the pile, which was taken by an increase in shaft resistance in the upper region (Figure 16). Figure 17 shows that pile 2 settled more in the lower portion of the pile than the soil in test TWPSI 2, hence the shaft resistance is expected to increase, with the observed reduction explained by a reduction of radial stress caused by tunnelling. The horizontal displacements in Figure 4 may help to explain this response, where a concentrated zone of horizontal displacement (directed towards the tunnel) is located in the lower region of piles 1 and 2 (caused by the bending of the 'deep' protective wall).

For pile 3 in all tests, the changes in pile head load are relatively small (Figure 13). However, there is some degree of load transfer along the length of the pile. For example, all three tests indicate an increase in shaft resistance in the upper portion of pile 3. This response may be related to some pile-pile interactions that occurred during the tests, which are more difficult to distinguish. An increase in shaft resistance in the upper portion of pile 4 is also observed from Figure 16, which goes against expectations since the pile was unloaded during tunnel volume loss in tests TPSI and TWPSI 1 (due to Mechanism S). Given the separation between pile 4 and the tunnel, this response can not be reasonably explained by any direct tunnel-pile interaction (i.e. Mechanism T); it is likely a result of pile-pile or wall-pile-pile interactions, or perhaps for pile 4 some influence of the centrifuge model boundary. A more detailed understanding of the pile-pile and wall-pile-pile interactions may be obtained through numerical modeling of the problem, which the authors aim to undertake in the future.

4. Summary and Conclusions

In this paper, results from four geotechnical centrifuge tests were presented to investigate the effect that protective walls have on reducing the impact of tunnelling on piled structures. Two protective walls with different embedded depths were used; a 'shallow' wall where the toe of the wall was located at the tunnel springline, and a 'deep' wall where the toe was located below the tunnel invert. An advanced hybrid testing technique, known as Coupled Centrifuge-Numerical Modeling (CCNM), was used to obtain an accurate replication of the tunnel-building interaction scenario, including fiber Bragg grating (FBG) strain sensors on the model walls and piles. The effect of the protective walls on soil displacements, pile settlements, structure deformations, pile head load transfer, and pile shaft resistance was discussed.

Soil displacement data indicated that 'deep' protective walls can significantly reduce the tunnelling induced ground movements on the retained side compared with the greenfield tunnelling case, whereas the effectiveness of the 'shallow' was minimal. The deformed shape of the protective wall depends on the length of the wall with respect to the depth of the tunnel; the 'shallow' wall predominately displayed rigid body rotation, whereas the 'deep' wall experienced bending within the middle portion of the wall.

It was shown that the 'deep' protective wall could significantly reduce pile settlement and structural distortions, even at relatively high tunnel volume losses approaching $V_{l,t} = 3\%$, whereas results from the 'shallow' wall were similar to those with no protective wall. Results from the numerical model run within the CCNM centrifuge tests demonstrated that the degree of panel distortion decreased with the increase in structure storey, with the building bay nearest the tunnel experiencing the greatest distortions, followed by the bay furthest from the tunnel.

The load transfer mechanisms among the piles, revealed using the FBG strain sensor data, showed that pile loading response could, in the main, be explained by mechanisms related to two mechanisms: Mechanism T related to tunnelling, and Mechanism S related to load redistribution within the building (a consequence of modeling building stiffness within the CCNM application). The pile nearest the tunnel experienced unloading at the pile tip as a result of ground stress relaxation related to tunnelling (even for the 'deep' protective wall, due to the bending action of the wall); the loss of load carrying capacity resulted in settlements for the 'shallow' and no-wall tests, with load being redistributed through the building to adjacent piles, whereas for the 'deep' wall, the pile was able to redistribute the lost load carrying capacity at its tip to the pile shaft, resulting in minimal pile settlement and negligible load redistribution within the building. In the 'shallow' and no-wall cases, load was mainly redistributed to the next pile along from the tunnel, which saw an increase in pile head load of about 11%.

5. NOTATION

B_{bay}	The spacing of bay
C	Depth of cover above the tunnel
C_u	Coefficient of uniformity
d_e	Distance between the pile and tunnel (Pile 1)
d_p	Diameter of the pile
d_w	Distance between the wall and tunnel
D_t	Diameter of the tunnel (d_t)
D_{50}	Average size of the soil particle
e_{max}	Maximum void ratio
e_{min}	Minimum void ratio
E	Young's modulus
EA	Axial stiffness
EI	Flexural rigidity
G_s	Specific gravity
H_{storey}	Height of the building storey in prototype scale
I_d	Relative density
L_p	Pile length, measured from ground surface to pile tip
L_w	Length of the protective wall
S_h	Horizontal displacement
S_p	Pile settlement

S_{pw} Pile settlement with the use of protective wall

S_s Pile settlement with structure only

S_t Spacing between piles

S_v Soil settlement; vertical displacement

t_w Thickness of the protective wall

$V_{l,t}$ Tunnel volume loss, in %

$V_{l,tf}$ Final tunnel volume loss, in %

z_t Depth of the tunnel

β Angular distortion parameter

$\Delta\lambda_B$ FBG wavelength shift

ϵ_{max} Maximum tensile strain

η_{pw} Efficiency parameter

$\overline{\eta_{pw}}$ Average efficiency parameter

θ Tile of the panel

ν Poisson's ratio

References

Bilotta, E., 2008. Use of diaphragm walls to mitigate ground movements induced by tunnelling. Géotechnique 58, 143–155.

Boone, S.J., 1996. Ground-movement-related building damage. Journal of Geotechnical Engineering 122, 886–896. doi:10.1061/(ASCE)0733-9410(1996)122:11(886).

Boscardin, M.D., Cording, E.J., 1989. Building response to excavation-induced settlement. Journal of Geotechnical Engineering 115, 1–21. doi:10.1061/(ASCE)0733-9410(1989)115:1(1).

Di Mariano, A., Gesto, J.M., Gens, A., Schwarz, H., 2007. Ground deformation and mitigating measures associated with the excavation of a new metro line, in: Proc. XIV European Conference on Soil Mechanics and Geotechnical Engineering, ECSMGE, pp. 1901–1906.

Elkayam, I., Klar, A., 2019. Nonlinear elastoplastic formulation for tunneling effects on superstructures. Canadian Geotechnical Journal 56, 956–969. doi:10.1139/cgj-2018-0021.

Farrell, R.P., 2010. Tunnelling in sands and the response of buildings. Ph.D. thesis. University of Cambridge.

Franza, A., 2016. Tunnelling and its effects on piles and piled structures. Ph.D. thesis. University of Nottingham.

Franza, A., Marshall, A.M., 2018a. Centrifuge and real-time hybrid testing of tunneling beneath piles and piled buildings. Journal of Geotechnical and Geoenvironmental Engineering 145, 04018110.

Franza, A., Marshall, A.M., 2018b. Centrifuge modelling study of the response of piled structures to tunnelling. ASCE Journal of Geotechnical and Geoenvironmental Engineering 144, 04017109.

Franza, A., Marshall, A.M., 2019. Empirical and semi-analytical methods for evaluating tunnelling-induced ground movements in sands. Tunnelling and Underground Space Technology 88, 47–62.

Franza, A., Marshall, A.M., Haji, T.K., Abdelatif, A.O., Carbonari, S., Morici, M., 2017. A simplified elastic analysis of tunnel-piled structure interaction. Tunneling and Underground Space Technology 61, 104–121. URL: http://dx.doi.org/10.1016/j.tust.2016.09.008, doi:10.1016/j.tust.2016.09.008.

Franza, A., Marshall, A.M., Zhou, B., 2019. Greenfield tunnelling in sands: the effects of soil density and relative depth. Geotechnique 69, 297–307. doi:10.1680/jgeot.17.p.091.

Gulvanessian, H., Formichi, P., Calgaro, J.A., 2009. Designers' Guide to Eurocode 1: Actions on Buildings: EN1991-1-1 and-1-3 TO-1-7. Thomas Telford Ltd.

Hibbitt, K., 2002. ABAQUS/Explicit User's Manual: Version 6.3. Hibbit, Karlsonn & Sorensen.

Hong, Y., Soomro, M.A., Ng, C.W.W., 2015. Settlement and load transfer mechanism of pile group due to side-by-side twin tunnelling. Computers and Geotechnics 64, 105–119. URL: http://linkinghub.elsevier.com/retrieve/pii/S0266352X14001906, doi:10.1016/j.compgeo.2014.10.007.

Idinyang, S., Franza, A., Heron, C., Marshall, A.M., 2018. Real-time data coupling for hybrid testing in a geotechnical centrifuge. International Journal of Physical Modelling in Geotechnics doi:doi.org/10.1680/jphmg.17.00063.

Jacobsz, S.W., 2003. The effects of tunnelling on piled foundations. Ph.D. thesis. University of Cambridge.

Kersey, A.D., Davis, M.A., Patrick, H.J., LeBlanc, M., Koo, K., Askins, C., Putnam, M., Friebele, E.J., 1997. Fiber grating sensors. Journal of lightwave technology 15, 1442–1463.

Ledesma, A., Alonso, E.E., 2017. Protecting sensitive constructions from tunnelling: the case of world heritage buildings in barcelona. Géotechnique 67, 914–925.

Lee, C.J., Wu, B.R., Chiou, S.Y., 1999. Soil movements around a tunnel in soft soils. Proc. Natl. Sci. Counc. ROC (A) 23, 235–247.

Marshall, A.M., 2009. Tunnelling in sand and its effect on pipelines and piles. Ph.D. thesis. University of Cambridge.

Marshall, A.M., 2012. Tunnel-pile interaction analysis using cavity expansion methods. Journal of Geotechnical and Geoenvironmental Engineering 138, 1237–1246.

Marshall, A.M., Mair, R.J., 2011. Tunneling beneath driven or jacked end-bearing piles in sand. Canadian Geotechnical Journal 48, 1757–1771.

Son, M., Cording, E.J., 2005. Estimation of building damage due to excavation-induced ground movements. Journal of Geotechnical and Geoenvironmental Engineering 131, 162–177.

Song, G., Marshall, A.M., 2020a. Centrifuge modelling of tunnelling induced ground displacements: pressure and displacement control tunnels. Tunnelling and Underground Space Technology 103, 103461. URL: http://www.sciencedirect.com/science/article/pii/S0886779820304156, doi:https://doi.org/10.1016/j.tust.2020.103461.

Song, G., Marshall, A.M., 2020b. A centrifuge study on the influence of tunnel excavation on piles in sand. ASCE Journal of the Geotechnical and Geoenvironmental Engineering 146, 04020129.

Song, G., Marshall, A.M., Heron, C., 2018. A mechanical displacement control model tunnel for simulating eccentric ground loss in the centrifuge, in: 9th International Conference of Physical Modelling in Geotechnics: ICPMG.

Song, G., Xu, J., Heron, C.H., Marshall, A.M., 2021. The application and calibration of fibre bragg grating for geotechnical centrifuge testings. International Journal of Physical Modelling in Geotechnics .

Stanier, S.A., Blaber, J., Take, W.A., White, D., 2015. Improved image-based deformation measurement for geotechnical applications. Canadian Geotechnical Journal 53, 727–739.

Vorster, T.E.B., 2006. The effects of tunnelling on buried pipes. Ph.D. thesis. University of Cambridge.

Xu, J., Franza, A., Marshall, A.M., 2020. Response of framed buildings on raft foundations to tunneling. Journal of Geotechnical and Geoenvironmental Engineering 146, 04020120. doi:10.1061/(ASCE)GT.1943-5606.0002376.

Zhou, B., 2015. Tunnelling-induced ground displacements in sand. Ph.D. thesis. University of Nottingham.